COLUMBIA UNDERGRADUATE SCIENCE JOURNAL

Unveiling Dark Matter in a Galaxy: A Case Study of NGC 1068

Seonyu Lee[1], Heeju Kim[1]

[1]Department of Physics and Astronomy, Seoul National University, Seoul, Republic of Korea

KEYWORDS: Dark matter distribution, SED fitting, galaxy photometry

ABSTRACT: The dark matter distribution in NGC 1068 is analyzed by determining its mass using dynamical mass from HI-based rotation curves and stellar mass from spectral energy distribution fitting of ugriz photometric data. High-precision photometry was achieved through Gaussian fitting, star masking, 3-sigma clipping, and error propagation, enabling robust flux measurements for spectral energy distribution analysis with CIGALE. Beyond 1.5 kpc, the dynamical mass begins to exceed the stellar mass. As the error bars do not overlap, the presence of dark matter is confirmed. The difference between the two masses is used to map the dark matter distribution from 1.5 kpc to 13 kpc. This study reproduces earlier findings using high-resolution data. Furthermore, the method for constraining dark matter distributions in individual galaxies and provides detailed spectral energy distribution results with uncertainties is refined.

INTRODUCTION

In the 1930s, astronomer Zwicky introduced the concept of “dark matter”, a form of matter that interacts gravitationally but not with light, while studying the Coma Cluster.[1] Later in the 1970s, Vera Rubin confirmed the existence of dark matter by revealing the flatness of galactic rotation curves.[2] Despite accumulating evidence of dark matter’s existence, its nature remains one of the most significant unsolved mysteries in modern astrophysics.

Astrophysicists have studied dark matter’s distribution and interaction with baryonic matter within the cosmic environment, uncovering characteristics of dark matter particles. These studies have focused on large-scale structures such as galaxy clusters.[3,4,5] However, investigating dark matter distribution within individual galaxies is equally important, as it provides valuable insights into galaxy formation and evolution and the interaction between dark and baryonic matter.[6,7] Additionally, galaxy simulations under various dark matter models can help elucidate its nature.[8,9]

This study presents a method for determining the dark matter distribution within a single galaxy, using NGC 1068 as a case study. As a Seyfert Type 2 galaxy, NGC 1068 hosts a heavily obscured active galactic nucleus (AGN), making it a valuable target for studying the interplay between dark matter, stellar populations, and AGN activity. Its well-documented structure and abundant multi-wavelength data allow for a detailed investigation of both baryonic and non-baryonic components. By comparing gravitational mass derived from rotation curves with stellar mass from spectral energy distribution (SED) fitting, this study reproduces historical findings providing the existence of dark matter. Rotation curves probe the total gravitational potential of a galaxy, while SED fitting constrains the stellar content based on photometry. Combining both enables us to isolate the dark matter component by comparing luminous and total mass distributions across different radii. Furthermore, it visualizes the radial distribution of dark matter within the galaxy.

For simplicity, the galaxy is modeled as a two-dimensional, axisymmetric plane. Although this ignores asymmetries, it helps us understand overall trends. Gravitational mass and its uncertainties are calculated from rotational curve data to map the gravitational mass distribution. Radial photometry is performed using optical filter FITS files, and photometric errors are calculated for SED fitting. The stellar mass and its uncertainty are derived from the best-fit parameters of the SED fitting process. These two methods collectively confirm the existence of dark matter, and the difference between the masses reveals the dark matter distribution, visualized as a colormap.

METHODS

Data

The observational data used in this study include FITS files of NGC 1068, captured with the ugriz filters using the LSGT at Siding Spring Observatory in Australia (Fig. 1). Additionally, the rotational curve data were employed, sourced from Brinks et al. (1997) [10]. This rotational curve consists of velocity measurements derived from HI emission lines et radii ranging from r = 20 arcsec to r = 180 arcsec (Fig. 2). The inclination of the galaxy is already corrected in the data, making this dataset well-suited for calculating the gravitational mass distribution across a broad radial range.

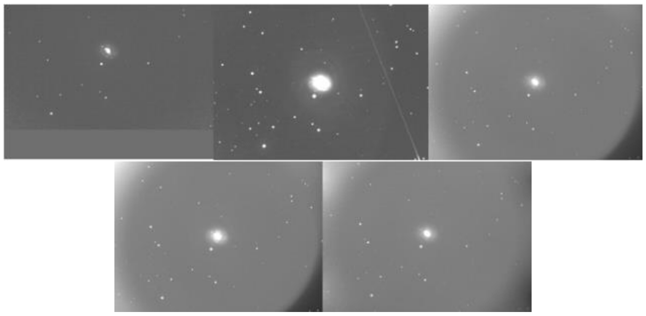

Figure 1. NGC 1068 imaged using ugriz filters with the LSGT.

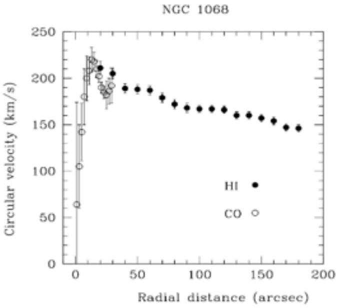

Figure 2. Rotation curve of NGC 1068.

Rotation curve

The rotation curve provides the distribution of velocities of stars and gas in a spiral galaxy as a function of radius, serving as a crucial tool for studying the galaxy's mass distribution and dynamics. From the rotation curve of NGC 1068 presented by Brinks et al. (1997), the velocities and their uncertainties were extracted at approximately 10 arcsecond intervals over the range r = 20 to 160 arcseconds.[10] Assuming a balance between centrifugal force and gravitational force according to Newtonian dynamics, the gravitational mass and its uncertainties were calculated using the following equation:

$$M = \frac{v^2 r}{G}, \qquad \frac{\Delta M}{M} = \frac{2\Delta v}{v}$$

SED fitting

SED fitting is a method used to optimize the flux emitted by galaxies across a broad range of wavelengths, from radio to X-ray. This technique provides insights into various physical properties of galaxies, such as star formation rate, star formation history (SFH), stellar mass, attenuation, dust mass and properties, metallicity, and active galactic nuclei (AGN). As a critical tool in galaxy studies, SED fitting enables the estimation of galaxy evolution, activity, formation epochs, and the characteristics of stars and interstellar material within galaxies.[11,12,13,14]

The effectiveness of SED fitting can be enhanced through two primary approaches. The first is conducting observations across the widest possible range of wavelengths.[15] Different wavelength ranges predominantly trace distinct components of a galaxy. For instance, radio wavelengths trace AGNs and star formation, while infrared reveals emissions from gas, dust, and older stars. Optical wavelengths capture stellar light, and X-rays highlight AGNs and hot gas.[16,17,18,19] Observing galaxies across a comprehensive wavelength range thus facilitates more accurate SED fitting and modeling.

The second approach involves refining the models used for SED fitting.[20] Current SED fitting software incorporates models and modules that represent various components, such as SFH, single stellar population (SSP), nebular emission, dust attenuation, dust emission, and AGNs. By adjusting the types of modules and input parameters, the models can be tailored for greater accuracy.

The key steps in SED fitting are as follows:

1. Acquiring galaxy flux measurements through multi-wavelength photometry.
2. Setting up models and input parameters.
3. Performing fitting using statistical algorithms.
4. Outputting the optimized SED and corresponding physical parameters.

Among the physical parameters provided by SED fitting programs are stellar mass and its Bayesian uncertainties. In this study, we employed SED fitting to derive stellar mass and its associated errors from galaxy photometric data.

CIGALE

CIGALE, short for Code Investigating GALaxy Emission, is a software designed for performing SED fitting. As a Python-based program, CIGALE offers lower technical complexity compared to other SED fitting tools and improves user accessibility with its automated features.[21,22] It also allows high flexibility by enabling users to configure various modules and input parameters, as well as exclude unnecessary modules. Despite limited observational data, CIGALE outputs the best-fit SED and parameters through sophisticated statistical analyses, such as chi-square minimization and Bayesian inference. For these reasons, this study employed CIGALE for SED fitting.[20]

CIGALE includes a wide range of modules for SFH, SSP, nebular emission, dust attenuation, dust emission, AGN, X-ray, radio, and redshift. However, since the observational data in this study is limited to the ugriz filters and optical wavelengths, only modules relevant to stellar emission were selected. The modules used in this study are listed below:

1. SFH: sfhdelayed.[23]
2. SSP: bc03.[11]
3. Nebular emission: nebular.[24]
4. Dust attenuation: dustatt_modified_CF00.[25]

Modules related to dust emission, AGN, x-ray, and radio were excluded due to the absence of corresponding observational data. The selected modules for SFH, SSP, nebular emission, and dust attenuation were chosen to yield the most reliable results given the limited dataset. Modules with fewer input parameters and simpler structures were prioritized. Input parameters for each module were configured by slightly expanding their default ranges.

The following steps summarize the workflow of CIGALE:

1. pcigale init: Create the config.ini file, which includes flux data for each filter, their measurement uncertainties, and module selections.
2. pcigale genconf: Configure the parameters for the selected modules.
3. pcigale check: Verify the parameter settings to ensure they are correctly configured before execution.
4. pcigale run: Generate all possible SED models based on the modules and parameters specified in config.ini, compare the models to the observed fluxes, select the model with the lowest chi-square value, and output the optimal SED model along with physical parameters.
5. pcigale-plots sed, pdf, chi2: Output graphs for the best-fit SED, parameter PDFs, and chi-square distributions.

CIGALE evaluates model fit quality and determines the optimal model using statistical techniques like chi-square minimization and Bayesian analysis. The chi-square computation incorporates a normalization factor for SFH, ensuring its integral equals one solar mass. This requires scaling the model values by a factor when calculating the chi-square.

$$\alpha = \frac{\sum_i \frac{f_i \times m_i}{\sigma_i^2}}{\sum_i \frac{m_i^2}{\sigma_i^2}} + \frac{\sum_j \frac{f_j \times m_j}{\sigma_j^2}}{\sum_j \frac{m_j^2}{\sigma_j^2}}$$

$$\chi^2 = \sum_i \left(\frac{f_i - \alpha \times m_i}{\sigma_i}\right)^2 + \sum_j \left(\frac{f_j - \alpha \times m_j}{\sigma_j}\right)^2 + \sum_k \left(\frac{f_k - m_k}{\sigma_k}\right)^2$$

Values with the subscript *i* represent the observed and model fluxes, while those with the subscript *j* denote observed and model parameters that depend on magnitude. Values with the subscript *k* correspond to observed and model parameters that are independent of magnitude. σ represents the observational uncertainties. CIGALE identifies the model with the smallest chi-squared value as the best-fit model and stores its corresponding SED graph and physical parameters in the results.fits and results.txt files.

While CIGALE identifies the optimal physical parameters by minimizing chi-square, galaxies with fundamentally different physical properties can exhibit similar SEDs. This issue becomes particularly challenging with limited observational data, as in this study.[20] To address this, CIGALE goes beyond parameter extraction by employing Bayesian analysis to derive probability distributions for each parameter. This process yields Bayesian mean values, Bayesian uncertainties, and confidence intervals for the parameters.

The Bayesian mean and confidence intervals are calculated using the following equations:

$$P(\Theta|D) = \frac{P(D|\Theta) \cdot P(\Theta)}{P(D)}$$

$$\langle\Theta\rangle = \frac{\int \Theta \cdot P(\Theta|D)\, d\Theta}{\int P(\Theta|D)\, d\Theta}$$

$$P(a \le \Theta \le b) = \int_a^b P(\Theta|D)\ d$$

Here, *D* represents the observational data, and θ represents the parameter of interest. In CIGALE's Bayesian framework, the likelihood

$P(\Theta|D)$ is weighted by the chi-square statistic.

$$P(D|\Theta) \propto e^{-\frac{1}{2}\chi^2}$$

Galaxy Photometry

After CIGALE input data required the redshift of NGC 1068, along with fluxes and their uncertainties in the ugriz filters at different radii. Since the initial values significantly impact CIGALE's results, accurate photometry and error estimation are essential. For NGC 1068, a redshift of z = 0.0038 was used.

Detecting the Center of the Galaxy

To identify the center of the galaxy, the surrounding stars and their associated background light were removed. This was achieved by averaging the brightness over small predefined regions and normalizing them to a uniform value. Subtracting the generated background from the original image resulted in a background-subtracted image. Additionally, excessively bright points were excluded to ensure accurate background estimation. This process was carried out using the photutils and astropy packages in Python.

The pixel coordinates with the maximum brightness were assumed to be the center of the galaxy. The brightness distribution was found to be sufficiently circularly symmetric based on the visualization of the galaxy's FITS file. Consequently, a 2D Gaussian fit was applied to model the peak in the symmetric distribution. The equation used for the Gaussian fitting is as follows:

$$f(x,y) = A \cdot \exp\left(-\left[\frac{(x-x_0)^2}{2\sigma_x^2} + \frac{(y-y_0)^2}{2\sigma_y^2}\right]\right) + C$$

The residual map indicated that pixel values near the center are close to zero (Fig. 3). These results verified the reliability of the Gaussian fitting, and the extracted coordinates were set as the center of the galaxy.

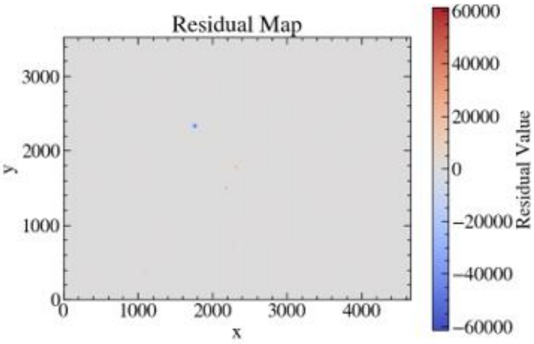

Figure 3. Residual map.

Masking star & radial photometry

To perform accurate photometry of the galaxy, bright stars within the aperture photometry region needed to be masked. Figure 4 shows the maximum photometry region used in this study and the masking of a bright star within that region. The center coordinates of the stars to be masked were identified, and the brightness of the detected star regions was replaced with pixel brightness corresponding to the background light.

The photometry radius was set to match the radii extracted from the rotation curve graph. As the galaxy was assumed to be circularly symmetric in this study, circular photometry was performed instead of elliptical photometry (Figure 5). The flux of the galaxy was calculated by summing the pixel brightness within the circular region and subtracting the background brightness times the area.

To convert the galaxy flux obtained in this manner into observational magnitudes, the following equation was used:

$$m = 22.5 - 2.5\log_{10}(F)$$

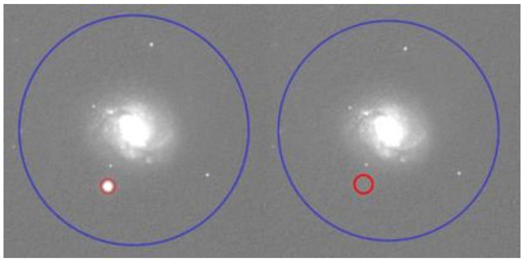

Figure 4. Stellar masking.

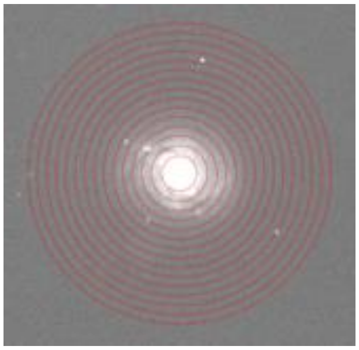

Figure 5. Radial circular photometry.

Secondary calibration

To derive the absolute flux from the observed data, standard stars within the dataset were identified. Their relative magnitudes were then compared to known absolute magnitudes to perform photometric calibration. However, the data in this study did not include standard stars. Thus, the right ascension (RA), declination (Dec), and relative magnitudes of stars were obtained and matched with SDSS data to determine absolute magnitudes (Figures 6, 7).[26]

Using the distribution of matched points, linear regression was applied to determine the values of k and ZP. To improve accuracy, outliers were removed using 3-sigma clipping (Figure 8). In 3-sigma clipping, points that deviate by more than three times the standard deviation from the distribution of other points are excluded. The equation used for this secondary calibration is as follows:

$$m_{\text{std}} - m_{\text{inst}} = k \cdot C_{\text{inst}} + \text{ZP}$$

$$C_{\text{inst}} = m_{i,\text{inst}} - m_{z,\text{inst}}$$

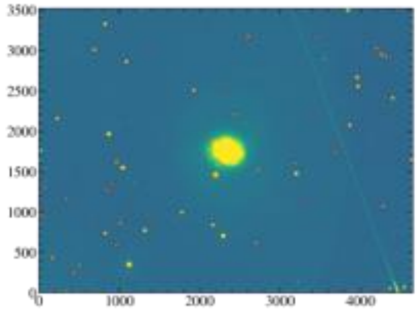

Figure 6. Star detection.

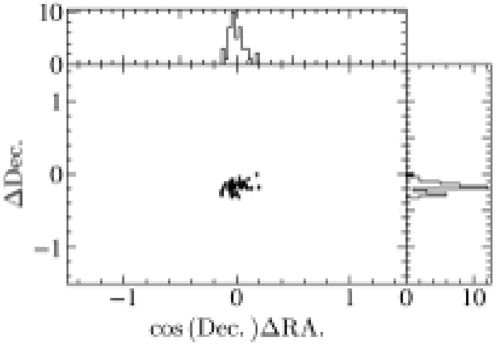

Figure 7. Matching errors in RA and Dec.

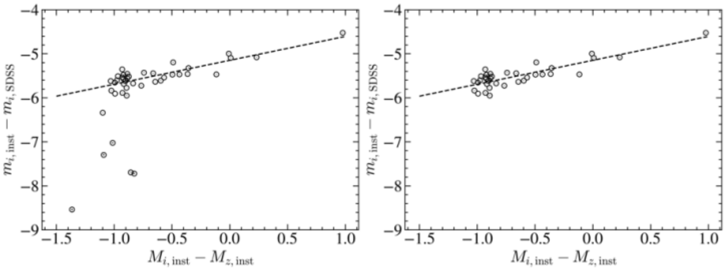

Figure 8. Before and after 3-sigma clipping.

Photometric error analysis

CIGALE requires input data in the form of fluxes and photometric uncertainties for each filter. The following equation was used to calculate magnitude uncertainties. The SNR represents the signal-to-noise ratio of the telescope, which was calculated assuming that the number of photons reaching the CCD follows a Poisson distribution.[27,28]

$$\text{SNR} = \frac{f_s}{\sqrt{f_s + f_{\text{bkg}}}}, \sigma_{m,\text{obj}} = \frac{2.5}{\ln(10) \cdot \text{SNR}}$$

The equation used to determine the uncertainty for secondary calibration is provided below.

$$\sigma_m = \sqrt{\left(\sigma_k(B-V)\right)^2 + (k\sigma_{B-V})^2 + \sigma_c^2 + \sigma_{m,\text{gal}}^2}$$

Lastly, the uncertainty arising from the process of converting absolute magnitudes into fluxes was calculated, with the value of f_0 set to $3.631*10^3$.

$$f = f_0 \cdot 10^{-0.4m}, \sigma_{\text{flux}} = \sigma_m \cdot 0.4\ln(10) \cdot f$$

The final total uncertainty was determined by summing the squares of these individual uncertainties and then taking the square root of the result.

RESULTS

Gravitational mass

The following graph shows the gravitational mass of NGC 1068 as a function of radius, calculated from its rotation curve. Error bars represent the uncertainties (Figure 9).

To visualize this in two dimensions, a circular colormap was used. The boundary of NGC 1068 was extracted from an image taken by the Hubble Space Telescope. The shape of the circular colormap was then adjusted to resemble the galaxy's image, and the two were overlaid for representation (Figure 10).

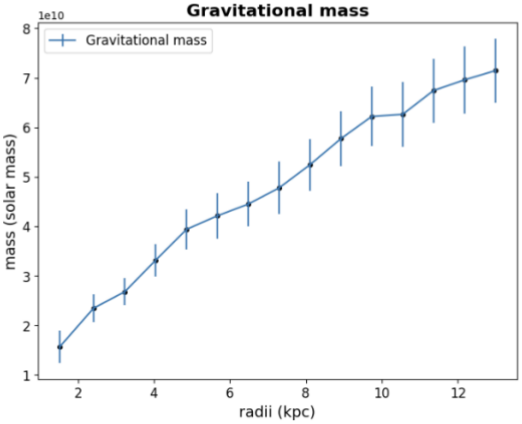

Figure 9. Gravitational mass distribution of NGC 1068.

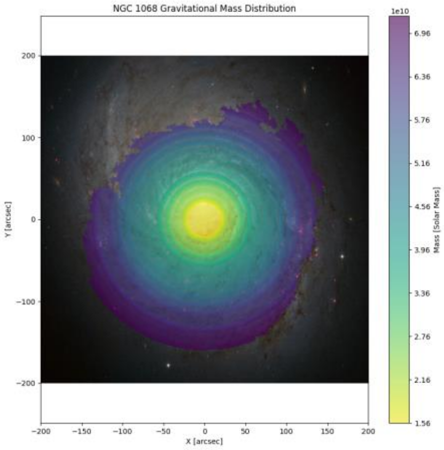

Figure 10. Colormap of the gravitational mass.

Photometry

From the results of linear regression for each filter, the values of *k* and ZP were obtained (Figure 11). Figure 12 shows the flux as a function of radius for each ugriz filter, presented in order from top to bottom as u, g, r, i, and z.

Comparing the observed flux in Jy units with data from the NASA Extragalactic Database (NED), it was found that the fluxes were smaller than those in NED: approximately 21% for the u-filter, 6% for the g-, r-, and i-filters, and 13% for the z-filter.

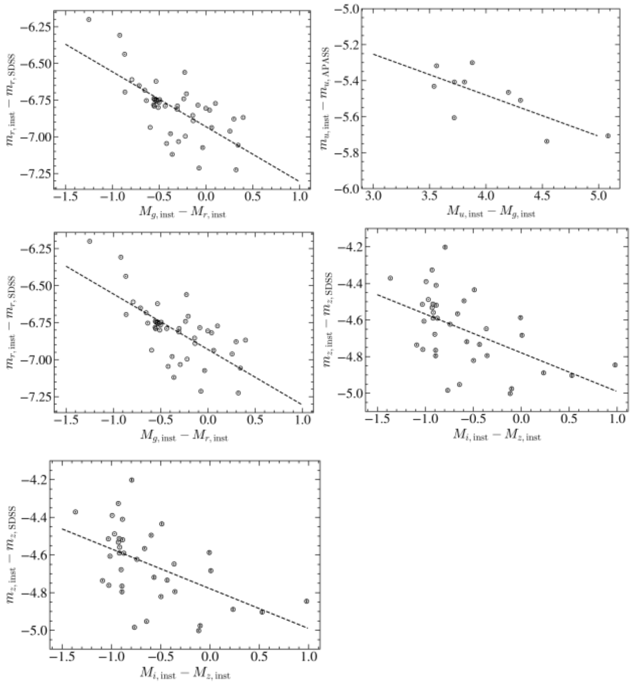

Figure 11. Linear regression results for the ugriz filters.

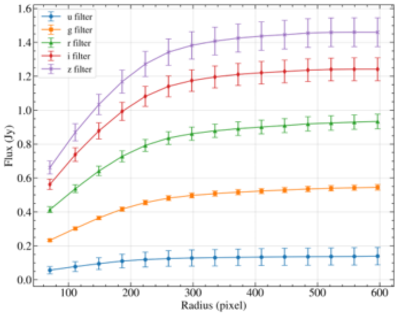

Figure 12. Flux as a function of radius for each ugriz filters (from top to bottom: u, g, r, i, z).

Stellar mass

The following results were obtained from running CIGALE, showing the best SED model for r = 1.5 kpc, the chi-squared distribution of stellar mass, the probability density function (PDF), and the radial distribution of stellar mass (Figures 13, 14, 15, 16, 17).

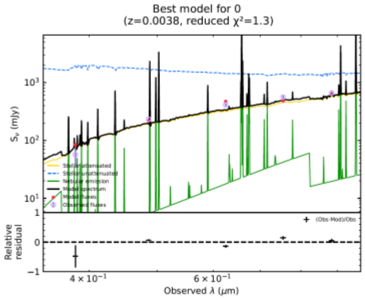

Figure 13. Best SED r = 1.5 kpc.

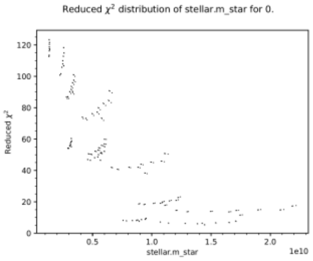

Figure 14. Chi-square distribution of stellar mass.

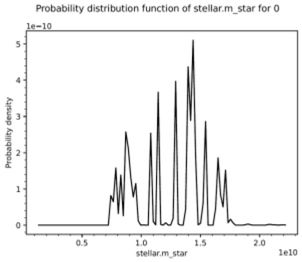

Figure 15: PDF of stellar mass r = 1.5 kpc.

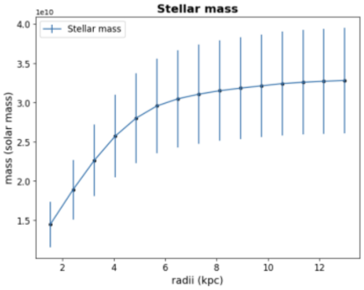

Figure 16. Stellar mass distribution of NGC 1068.

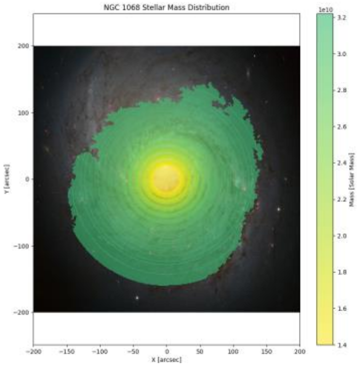

Figure 17. Colormap of the stellar mass distribution.

Dark Matter

The difference between gravitational and stellar mass increases with radius, and their 1σ error bars do not overlap beyond 1.5 kpc (Fig. 18), indicating a statistically significant discrepancy. This excess of gravitational mass relative to stellar mass is consistent with the presence of dark matter. The trend remains robust across the full radial range considered. This provides further evidence for the existence of dark matter, which interacts gravitationally but not electromagnetically, as revealed through dynamical analysis. Figures 19 and 20 present the resulting dark matter mass distribution of NGC 1068.

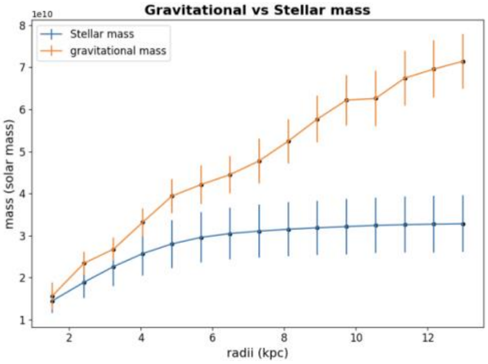

Figure 18. Gravitational mass vs Stellar mass in NGC 1068.

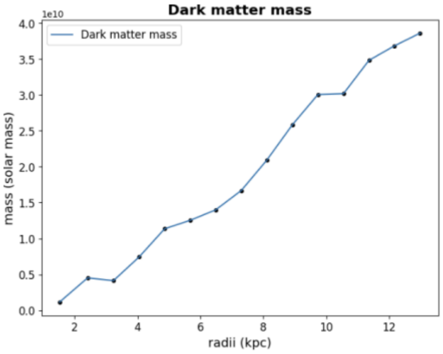

Figure 19. Dark matter mass distribution of NGC 1068.

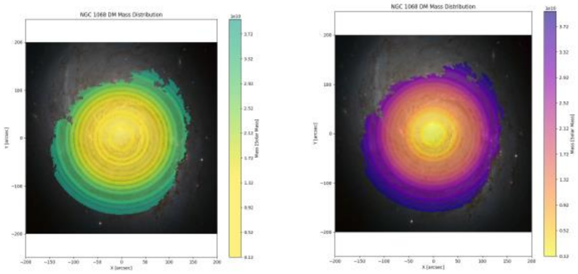

Figure 20. Dark matter colormap of NGC 1068.

DISCUSSION

Results of CIGALE

The residual map from the SED fitting shows that the error bars for the u-filter are abnormally large compared to other filters. This discrepancy likely stems from issues with the u-filter data or from fewer stars being detected during secondary calibration, compared to other filters. Given that the LSGT has a relatively small apertures of 0.43m, the accuracy of u-filter observations may have been low, even with longer exposure times.

Furthermore, the flux of galaxies and stars in the u-filter was observed to be smaller than in other filters. This could have introduced significant errors during the linear regression or background light subtraction processes.

Using a high-performance telescope would allow for more refined and accurate analyses. These enhancements could address the limitations identified above.

Dark matter mass estimation

Dark matter mass is typically calculated as the difference between the total dynamical mass of a galaxy and the combined mass of its stars and gas. However, in this study, gas mass was not included due to the lack of observational data in the radio and infrared wavelengths, where gas emissions are primarily detected. Estimating gas mass using optical data alone is unreliable and could lead to inaccurate results.[29,30] Additionally, the CIGALE modules for dust emission were omitted, further limiting the analysis. As a result, the dark matter mass estimation in this study considered only stellar mass, representing a key limitation.

The graph comparing gravitational mass and stellar mass indicates that the two are nearly identical in the central region, suggesting that dark matter is absent within approximately r = 1.5 kpc. This observation is another limitation of this study. NGC 1068 is a galaxy with strong AGN emissions at its center, but no AGN-related modules were configured in CIGALE. As a result, AGN emissions may have been misinterpreted as stellar emissions during the SED fitting process, leading to an overestimation of the stellar mass in the central region.[31,32] This issue is further exacerbated by the lack of infrared and AGN-related data, which led to the exclusion of relevant CIGALE modules—such as AGN, dust, and radio. Consequently, the stellar mass is likely overestimated in AGN-dominated regions, biasing the dark matter estimates within ~1.5 kpc. Since AGN emissions are predominantly observed in X-ray and radio wavelengths, which were not included in this study, likely contributing to the issue.

Securing observational data in the radio and X-ray wavelengths could address the limitations discussed above.

SED fitting in previous studies typically incorporates observational data across a broad wavelength range, using measurements from approximately 10 to 20 filters. In contrast, this study relied on data from a narrow wavelength range and only five filters, which posed significant limitations. Consequently, the reliability of the dark matter mass distribution results is likely affected.

CONCLUSION

This study demonstrated the existence of dark matter and determined its distribution within a single galaxy, NGC 1068, using photometric data from the LSGT and its rotation curve.

Gravitational mass and its uncertainties were calculated from the rotation curve, and photometric data were generated to perform SED fitting with CIGALE. To ensure accurate photometric data, the study involved four key processes: identifying the galaxy's center, masking bright surrounding stars, conducting secondary calibration, and calculating photometric uncertainties through signal-to-noise ratio analysis and error propagation. From the SED fitting results, the optimal stellar mass and Bayesian errors were obtained. A comparison between the calculated stellar mass and gravitational mass confirmed the presence of dark matter, which cannot be observed through electromagnetic waves. Radial photometry was performed, and SED fitting results were obtained for each radius, allowing the determination of the dark matter distribution.

This study proposed a method for determining the dark matter mass distribution within a single galaxy, which can contribute to refining known dark matter density profiles (e.g. the NFW profile). Additionally, the results provide valuable insights into galaxy formation and evolution.

The significance of this study lies in its focus on a single galaxy. This offers a new direction for dark matter research, which has traditionally focused on larger-scale structures like galaxy clusters.

AUTHOR INFORMATION

Corresponding Author

Seonyu Lee – julius712@snu.ac.kr

Author Contributions

Seonyu Lee led the research from conception to execution, including designing the study, analyzing results, and writing the manuscript. Heeju Kim contributed to the photometric data analysis and data processing.

REFERENCES

[1] F. Zwicky, Die Rotverschiebung von extragalaktischen Nebeln. *Helv. Phys. Acta*. 6, 110-127 (1933). https://doi.org/10.5169/seals-110267

[2] V. C. Rubin, W. Ford, Jr. Kent, Rotation of the Andromeda Nebula from a spectroscopic survey of emission regions. *ApJ* 159, 379 (1970). https://doi.org/10.1086/150317

[3] M. Markevitch, *et al*., Direct constraints on the dark matter self-interaction cross. *ApJ* 606(2), 819-824 (2004). https://doi.org/10.1086/383178

[4] D. Clowe, *et al*., A direct empirical proof of the existence of dark matter. *ApJ* 648(2), L109-L113 (2006). https://doi.org/10.1086/508162

[5] M. A. Henson, D. J. Barnes, S. T. Kay, I. G. McCarthy, J. Schaye, The impact of baryons on massive galaxy clusters: halo structure and cluster mass estimates. *MNRAS*, 465(3), 3361-3378 (2017). https://doi.org/10.1093/mnras/stw2899

[6] K. G. Begeman, HI rotation curves of spiral galaxies. I. NGC 3198. *A&A* 223, 47-60 (1989).

[7] A. A. Dutton, A. V. Maccio, Cold dark matter haloes in the Planck era: evolution of structural parameters for Einasto and NFW profiles. *MNRAS* 441(4), 3359-3374 (2014). https://doi.org/10.1093/mnras/stu742

[8] V. Springel, et al., Simulations of the formation, evolution and clustering of galaxies and quasars. *Nature* 435(7042), 629-636 (2005). https://doi.org/10.1038/nature03597

[9] J. S. Bullock, M. Boylan-Kolchin, Small-scale challenges to the ΛCDM paradigm. *Annu. Rev. Astron. Astrophys*. 55, 343-387 (2017). https://doi.org/10.1146/annurev-astro-091916-055313

[10] E. Brinks, E. D. Skillman, R. J. Terlevich, E. Terlevich, HI Observations of NGC 1068. *Astrophys. Space. Sci.* 248, 23-31 (1997).

[11] G. Bruzual, S. Charlot, Stellar population synthesis at the resolution of 2003. *MNRAS* 344(4), 1000-1028 (2003). https://doi.org/10.1046/j.1365-8711.2003.06897.x

[12] D. Le Borgne, *et al*., Evolutionary synthesis of galaxies at high spectral resolution with the code PEGASE-HR. *A&A* 425, 881-897 (2004). https://doi.org/10.1051/0004-6361:200400044

[13] C. Conroy, Modeling the panchromatic spectral energy distributions of galaxies. *Annu. Rev. Astron. Astrophys*. 51, 393-455 (2013). https://doi.org/10.1146/annurev-astro-082812-141017

[14] C. Pacifici, *et al.*, The evolution of star formation histories of quiescent galaxies. *ApJ* 832(1), 79 (2016). https://doi.org/10.3847/0004-637X/832/1/79

[15] J. Walcher, B. Groves, T. Budavari, D. Dale, Fitting the integrated spectral energy distributions of galaxies. *Astrophys. Space. Sci.* 331(1), 1-51 (2011). https://doi.org/10.1007/s10509-010-0458-z

[16] J. J. Condon, Radio emission from normal galaxies. *Annu. Rev. Astron. Astrophys*. 30, 575-611 (1992). https://doi.org/10.1146/annurev.aa.30.090192.003043

[17] R. C. Kennicutt Jr., Star formation in galaxies along the Hubble sequence. *Annu. Rev. Astron. Astrophys.* 36, 189-232 (1998). https://doi.org/10.1146/annurev.astro.36.1.189

[18] K. Nandra, P. M. O’Neill, I. M. George, J. N. Reeves, An XMM-Newton survey of broad iron lines in Seyfert galaxies. *MNRAS* 382(1), 194-228 (2007). https://doi.org/10.1111/j.1365-2966.2007.12331.x

[19] S. Bianchi, E. M. Xilouris, The extent of dust in NGC 891 from Herschel/SPIRE images. *A&A* 531, L11 (2011). https://doi.org/10.1051/0004-6361/201116772

[20] M. Boquien, *et al*., CIGALE: a python Code Investigating GALaxy Emission. *A&A* 622, A103 (2019). https://doi.org/10.1051/0004-6361/201834156

[21] E. da Cunha, S. Charlot, D. Elbaz, A simple model to interpret the ultraviolet, optical and infrared emission from galaxies. *MNRAS* 388(4), 1595-1617 (2008). https://doi.org/10.1111/j.1365-2966.2008.13535.x

[22]C. Conroy, J. E. Gunn, M. White, The propagation of uncertainties in stellar population synthesis modeling. I. The relevance of uncertain aspects of stellar evolution and the initial mass function to the derived physical properties of galaxies. *ApJ* 699(1), 486-506 (2009). https://doi.org/10.1088/0004-637X/699/1/486

[23]K. Malek, *et al.*, HELP: modelling the spectral energy distributions of Herschel detected galaxies in the ELAIS N1 filed. *A&A* 620, A50 (2018). https://doi.org/10.1051/0004-6361/201833131

[24]A. K. Inoue, Rest-frame ultraviolet-to-optical spectral characteristics of extremely metal-poor and metal-free galaxies. *MNRAS* 415(3), 2920-2931 (2011). https://doi.org/10.1111/j.1365-2966.2011.18906.x

[25]S. Charlot, S. M. Fall, A simple model for the absorption of starlight by dust in galaxies. *ApJ* 539(2), 718-731 (2000). https://doi.org/10.1086/309250

[26]A. Meiksin, colour corrections for high-redshift objects due to intergalactic attenuation. *MNRAS* 365(3), 807-812 (2006). https://doi.org/10.1111/j.1365-2966.2005.09756.x

[27]B. M. Tinsley, Evolution of the stars and gas in galaxies. Fundam. Cosmic Phys. 5, 287-388 (1980). https://doi.org/10.48550/arXiv.2203.02041

[28]N. Gehrels, Confidence limits for small numbers of events in astrophysical data. *ApJ* 303, 336 (1986). https://doi.org/10.1086/164079

[29]J. R. Taylor, *An Introduction to Error Analysis: The Study of Uncertainties in Physical Measurements* (University Science Books, 1997).

[30]A. K. Leroy, *et al.*, The star formation efficiency in nearby galaxies: measuring where gas forms stars effectively. *Astron J* 136(6), 2782-2845 (2008). https://doi.org/10.1088/0004-6256/136/6/2782

[31]K. Iwasawa, A. C. Fabian, A. J. Young, H. Inoue, C. Matsumoto, Variation of the broad X-ray iron line in MCG-6-30-15 during a flare. *Mon. Not. R. Astron. Soc.* 306, L19-L24 (1999).

[32]M. Polleta, Spectral energy distributions of hard X-ray selected active galactic nuclei in the XMM-Newton medium deep survey. *ApJ* 663(1), 81-102 (2007). https://doi.org/10.1086/518113